

Numerical methods for determining the kinematics of coronal mass ejections and coronal waves

J.P. Byrne¹, D.M. Long², P.T. Gallagher³, S.A. Maloney^{?4}, S.D. Bloomfield^{?3}, H. Morgan^{5,1}, and S.R. Habbal¹

¹ Institute for Astronomy, University of Hawai'i, 2680 Woodlawn Drive, Honolulu, HI 96822, USA.
e-mail: jbyrne@ifa.hawaii.edu

² UCL–Mullard Space Science Laboratory, Holmbury St. Mary, Dorking, Surrey, RH5 6NT, UK.

³ School of Physics, Trinity College Dublin, College Green, Dublin 2, Ireland.

⁴ Skytek, 51/52 Fitzwilliam Square West, Dublin 2, Ireland

⁵ Institute of Mathematics and Physics, Aberystwyth University, Ceredigion, SY23 3BZ, UK.

Received ?; accepted ?

ABSTRACT

Context. Why are we doing this work?

Aims. In this paper we show that traditional techniques for the determination of CME and “EIT wave” kinematics, as currently applied, do not return accurate estimates of the true kinematics of the feature. We highlight the errors inherent in these approaches and illustrate a recipe for accurate estimates of the kinematics using a residual resampling bootstrapping approach to determine the confidence interval associated with the model used to measure them.

Methods. We discuss the errors inherent in the use of numerical differentiation techniques when applied to small data-sets. We present a residual resampling bootstrapping approach as a statistically rigorous technique for the determination of accurate kinematic estimates.

Results. It is shown that accurate feature kinematics can only be estimated by applying a pre-determined model to the position measurements. The validity of this model must be based on the physical properties of the feature that are to be measured, and the accuracy of applying that model to the data can be examined using a bootstrapping approach to determine the confidence interval associated with the estimated model parameters.

Conclusions. What are our conclusions?

Key words. Sun: activity – Sun: corona – Sun: coronal mass ejections (CMEs)

1. Introduction

The most defining feature of a transient solar phenomenon such as a Coronal Mass Ejection (CME) or a coronal wave (commonly called an “EIT Wave”) is its motion. These generally short-lived features, resulting from a solar eruption, are observed to propagate across the solar corona (i.e., coronal waves) or in the case of CMEs, outward from the Sun into the heliosphere. Observational catalogues of both phenomena have been compiled over more than \sim 20 years of observations (e.g., Illing & Hundhausen, 1985; Yashiro et al., 2004; Thompson & Myers, 2009), with the physical properties of both phenomena very well characterised (see the recent reviews by e.g., Gallagher & Long, 2011; Patsourakos & Vourlidas, 2012; Howard, 2011; Webb & Howard, 2012).

As transient phenomena, the kinematics of both sets of features continue to be one of the most important characteristics used to classify them. The motion of both phenomena is traditionally identified using difference images, where a preceding image is subtracted from a leading image to highlight motion, allowing the feature to be identified “by eye”. However, this approach highlights *relative* rather than *actual* motion, and is prone to undefined user-dependent bias. More recent work has used single image processing techniques such as wavelet transforms (Byrne et al., 2009;

Morgan et al., 2012) and automated approaches (e.g., Long et al., 2011; Byrne et al., 2012; Podladchikova et al., 2012) to minimise user-error and reveal the true physical characteristics of the feature. By tracking the position of the feature with time it is possible to determine its kinematics, allowing an insight into the physical properties of the phenomenon.

The kinematics of these features are important for a variety of reasons. The true physical nature of coronal waves is not fully understood, with two main competing theories; that they are waves (e.g., Shen & Liu, 2012; Veronig et al., 2010) or signatures of magnetic field restructuring during a CME eruption (e.g., Schrijver et al., 2011; Chen & Wu, 2011). The kinematics of the feature have been proposed as one of the main discriminators between these competing theories, with the relatively high velocities measured thus far for this phenomenon suggesting a wave interpretation may be appropriate (cf. Warmuth & Mann, 2011; Zheng et al., 2012). Similarly, CME kinematics are vitally important from a space weather point of view as they allow increased accuracy in the predicted arrival time of the feature at Earth. The kinematic behaviour of the CME very low down in the solar corona may also be used to discriminate between eruption mechanisms (cf. Lin et al., 2010). However Wen et al. (2007) demonstrate that the errors in

CME acceleration values can be of the same order as the accelerations typically measured.

A variety of different mathematical techniques exist for deriving the kinematics of transient features, ranging from the fitting of polynomial functions to the distance-time measurements to the numerical differentiation of the measurements. While these techniques may be mathematically sound, some of them are not necessarily applicable to the derivation of kinematics for these features and can produce spurious results.

2. Numerical Differentiation & Error Propagation (recap)

When presented with a moving object through a sequence of image frames such that it is possible to measure its position at each time step, the technique of numerical differentiation is often used to derive the velocity and acceleration of the object. In the standard 2-point approach, it should be possible to derive the time evolution of a system at time step $t+\delta t$ according to the system values at time step t . This may be applied through the technique of forward, reverse or centre differencing, resulting in an estimate of the speed of the object at a specific time step given its positional information. More commonly, a 3-point Lagrangian interpolation is applied to better approximate the kinematics of a moving object by solving for the Lagrange polynomials that best fit across three given datapoints (e.g. DERIV.PRO in IDL). Each of these schemes is based upon the Taylor series expansion of a real function $f(t)$:

$$f(t_0 + \delta t) = f(t_0) + f'(t_0)\delta t + \frac{f''(t_0)}{2!}(\delta t)^2 + \dots \quad (1)$$

but due to the approximation of an infinite series with a finite number of terms and iterations, an error must be associated with the result, based on its deviation from the true solution. Generally the Euler method is employed, using the formula:

$$y_{n+1} = y_n + h f(t_n, y_n) \quad (2)$$

to solve the initial value problem $y' = f(t, y)$ given $y(t_0) = y_0$, where h is the stepsize such that $t_n = t_0 + nh$. The convergence of such an approximation to the actual solution is prone to two sources of error; truncation error (the difference between the true solution and the approximation) and round-off error (the limited precision of the approximation). Added to this is the fact that the data measurements themselves are subject to uncertainties in both the positional and temporal information, and the ability of the numerical differentiation techniques to derive kinematics becomes highly jeopardised, as shall be shown.

Given a function $x = f(u, v)$, the error propagation equation (based on the standard deviations σ of the variables) is written:

$$\sigma_x^2 = \sigma_u^2 \left(\frac{\partial x}{\partial u} \right)^2 + \sigma_v^2 \left(\frac{\partial x}{\partial v} \right)^2 + 2\sigma_{uv}^2 \left(\frac{\partial x}{\partial u} \right) \left(\frac{\partial x}{\partial v} \right) + \dots \quad (3)$$

Specifically in the case of kinematic analyses, this is used to propagate the errors on the distance-time data $r(t)$ into the velocity $v(t)$ and acceleration $a(t)$ profiles to determine the associated uncertainties. In the case of distance-time

data the covariance terms are zero because the quantities are uncorrelated.

When presented with relatively low sampling of the data, as in the case of coronagraph observations of CMEs and disk observations of waves, it is generally found that the simplest differentiation techniques are not applicable. The forward and/or reverse differencing techniques act to shift the kinematic profiles by one time-step, which is substantial enough to be of concern here (i.e., they derive a result at the current time-step, based on the pro-/preceding time-step). Centre differencing employs the two neighbouring data-points of the point under examination, and so is a better indication of the result at that time-step, but it fails at both endpoints. In any case these should not be employed when the spacing of the data-points is unequal, i.e., when the cadence δt is not constant, and so the 3-point Lagrangian interpolation technique is used (which gives the same result as the centre-difference otherwise, but includes the endpoints and has an associated error propagation formulation). The Lagrangian interpolation polynomial is given by:

$$L(x) = \sum_{j=0}^2 y_j l_j(x) \quad (4)$$

$$\text{where } l_j(x) = \prod_{i=0, i \neq j}^2 \frac{x - x_i}{x_j - x_i} \quad (5)$$

The derivative at point x is given by $L' = \partial_x L(x)$. So for the case of height-time data being used to derive velocity (and similarly acceleration) the associated error is given by:

$$\sigma_{v_1}^2 = \frac{\sigma_{r(t_2)}^2 + \sigma_{r(t_0)}^2}{(t_2 - t_0)^2} + v^2 \left(\frac{\sigma_{t_2}^2 + \sigma_{t_0}^2}{(t_2 - t_0)^2} \right) \quad (6)$$

as in DERIVSIG.PRO in IDL. The endpoint errors are derived from a weighting of the pro/preceding two data-points, that is therefore larger to reflect the unknown nature of the trend beyond the sample points.

Although the 3-point Lagrangian is mathematically sound, its application to solar eruptive event kinematics proves problematic. The main drawbacks are two-fold:

1. The noise level, especially across low-cadence sampling, can scatter the measurements to such a degree that the numerical derivatives become untrustworthy and even misleading compared to the actual trends of the kinematic data.
2. The error-propagation formulation results in a misleading uncertainty interval on the velocity and acceleration profiles. For example, it counter-intuitively increases for increasing cadence measurements.

Simulations of the drawbacks of a standard numerical derivative are presented in Section 3. In Section 4 we outline a more appropriate method for inspecting the kinematics of CMEs and waves, as applied to model data. In Section 5 some real-data cases are revisited with these methods, and motivate the proposed treatment of data from the new coronal image processing CME catalogue (CORIMP; [Morgan et al., 2012](#); [Byrne et al., 2012](#)), and coronal pulse identification and tracking algorithm catalogue (CorPITA; [Long et al., 2011](#)). A final discussion and conclusions are presented in Section 6.

3. Simulations

In the case of CMEs and waves, there is great motivation to resolve the dynamics of their propagation as pre-

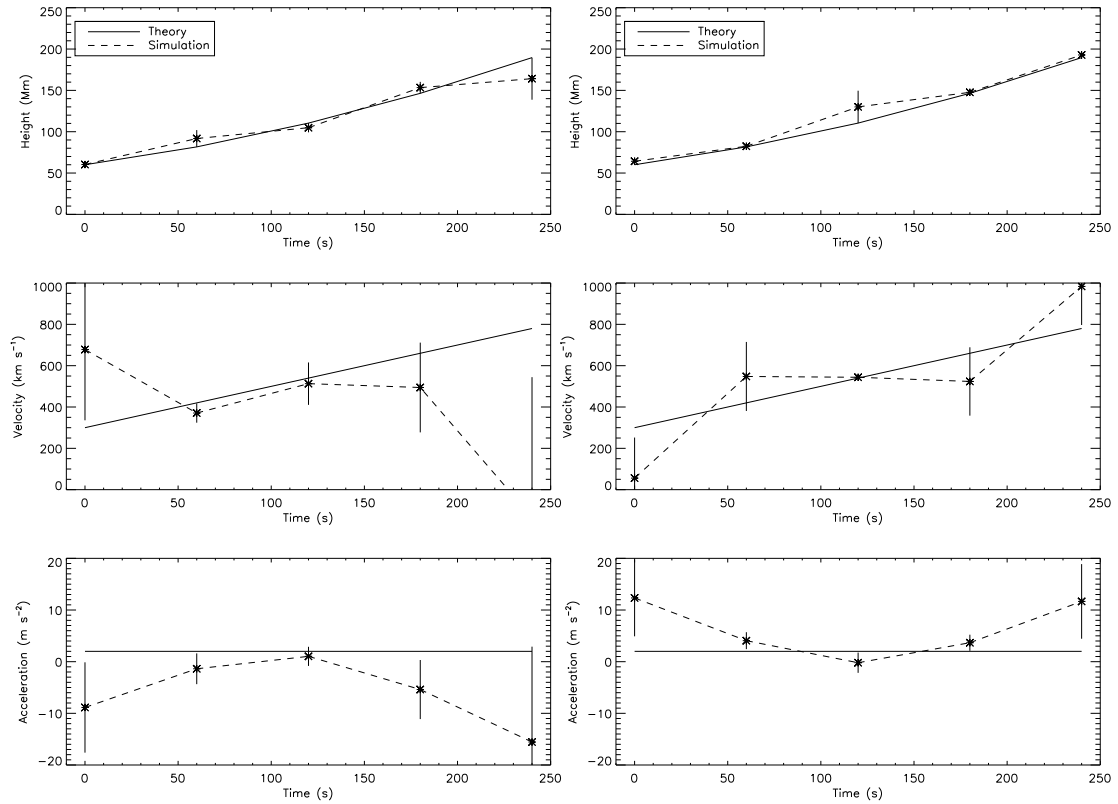


Fig. 1. A theoretical model for a CME with constant acceleration 2 m s^{-2} and initial velocity 300 km s^{-1} , and two simulations of how the resulting profiles for a noisy sample of data-points behave using 3-point Lagrangian interpolation.

cisely as possible in order to study the forces at play. For example, CMEs in general may be undergoing continued driving (internal) forces, or positive or negative drag (external) forces, or most assuredly some interplay of both. Similarly wave propagation may be affected by changes to the low-coronal environs, e.g., low-density coronal hole regions. Thus any changes to event acceleration that result from different phases of dominating force, and where or why this can occur, are of great interest. But this all remains somewhat elusive given the inherent limitations of the data and the numerical methods employed. In our treatment of both phenomena here, we use cases of simulated CME and wave data interchangeably, and demonstrate both constant and non-constant acceleration profiles with varying scatter and cadence.

3.1. Effect of scatter/noise on deriving kinematics

As an example of the effect of noise, we first simulate a simple height-time profile of a CME that propagates according to the quadratic equation:

$$r(t) = r_0 + v_0 t + \frac{1}{2} a t^2 \quad (7)$$

where $r_0 = 60 \text{ Mm}$ is the initial height, $v_0 = 300 \text{ km s}^{-1}$ is the initial velocity, and $a = 2 \text{ m s}^{-2}$ is the acceleration of the CME. Varying levels of noise are randomly added up to a maximum of 20 %. An ‘extreme case’ errorbar on each datapoint is determined by its distance from the true height-time profile, to represent a scenario wherein all measurement uncertainties just manage to overlap the true profile. Various instances of randomized datapoint scatters result in

erroneous trends in the velocity and acceleration profiles, even with the proper error treatment ascribed by the 3-point Lagrangian interpolation technique, and even in this simplest case of constant acceleration. Two examples are shown in the left and right of Figure 1 where completely opposing acceleration trends are determined for different samplings of the same dataset, indicating that the nature of the scatter in the samples is not satisfactorily reflected in the derived kinematics and their associated errors. At the very least the error bars should be expected to overlap the truth in each plot so that it remains a valid solution. A possible assurance, even in the case of low-cadence samplings (or very fast events), is that instead of trusting the endpoints they simply be removed. Figure 1 would then show three datapoints for velocity and one datapoint for acceleration, that would go somewhat toward removing the biased trends and imply a constant acceleration close to the true value. However, when dealing with low-number samples especially, it would be better not to have to remove datapoints.

The effects of varying uncertainty in the data of a coronal wave were also examined, demonstrated here for the case of a constant acceleration event. The wave motion is modeled by Equation 7, where $r_0 = 50 \text{ Mm}$ is the initial distance of the wave from the source, $v_0 = 400 \text{ km s}^{-1}$ is the initial velocity of the wave, and $a = -150 \text{ m s}^{-2}$ is the acceleration of the wave. Figure 2 shows the derived kinematics for the simulated dataset with noise levels of 20 % (top), 10 % (middle) and 5 % (bottom). A quadratic is then fit to each dataset, showing how the variation due to the noise level has a noticeable effect on the derived kinematics in

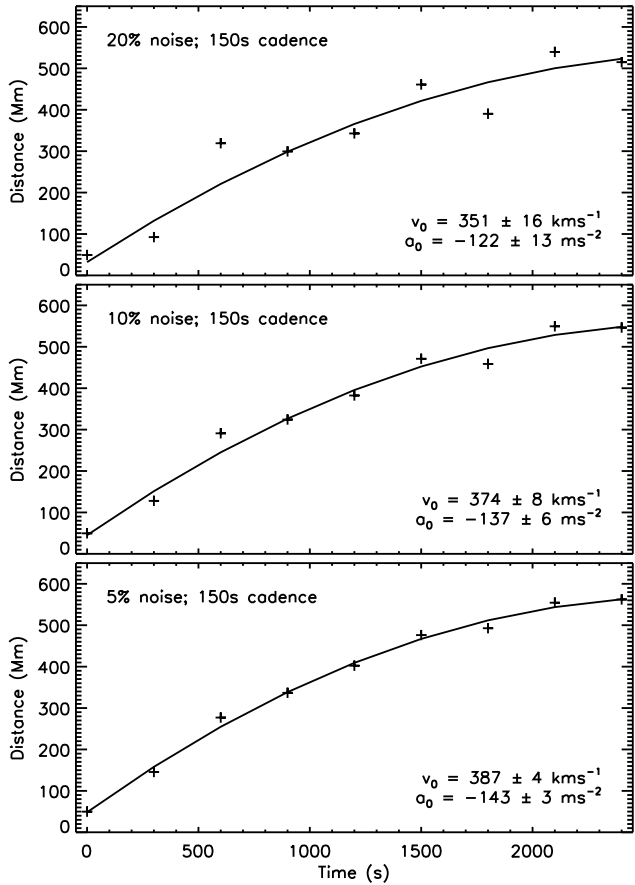


Fig. 2. Simulated data (crosses) for noise distributions with widths of $\pm 20\%$ (top), $\pm 10\%$ (middle) and $\pm 5\%$ (bottom) of the data value. In each case, the fit to the data is shown in red with derived kinematics in the bottom right of each panel.

each case, with the acceleration in particular exhibiting significant deviation when the scatter is increased.

The variation in the derived kinematics for varying levels of scatter is shown in Figure 3, showing the determined distance (r_0), initial velocity (v_0) and acceleration (a_0) in the top, middle and bottom panels respectively. The degree to which the scatter affects the fits is apparent, with dramatic offsets from as little as 5 % noise, further enhanced for the derived velocities and accelerations.

3.2. Effect of sampling cadence on deriving kinematics

As an example of the effect of cadence, we first simulate a non-constant acceleration profile for a CME via the following equations (where the constant x is just a scaling factor):

$$h(t) = \sqrt{2x} t \tan^{-1} \left(\frac{e^{t/2x}}{\sqrt{2x}} \right) \quad (8)$$

$$v(t) = \sqrt{2x} \tan^{-1} \left(\frac{e^{t/2x}}{\sqrt{2x}} \right) + \frac{e^{t/2x} t}{e^{t/x} + 2x} \quad (9)$$

$$a(t) = \frac{e^{t/2x} (2x(t+4x) - e^{t/x}(t-4x))}{2x(e^{t/x} + 2x)^2} \quad (10)$$

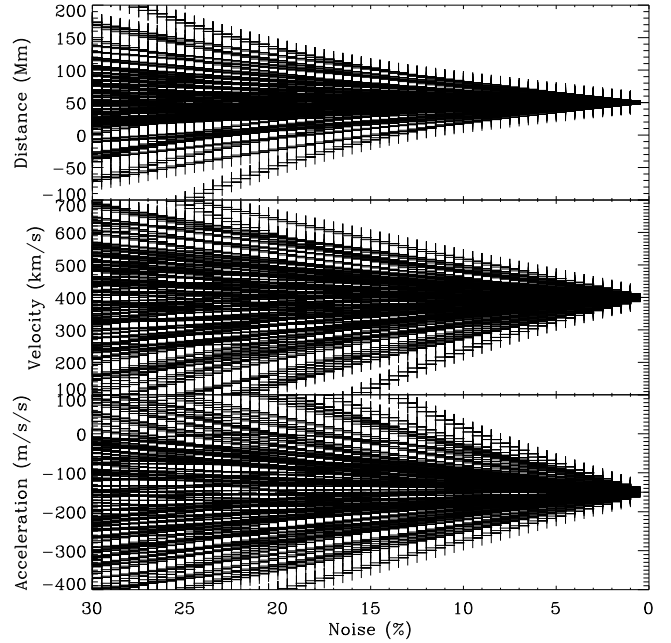
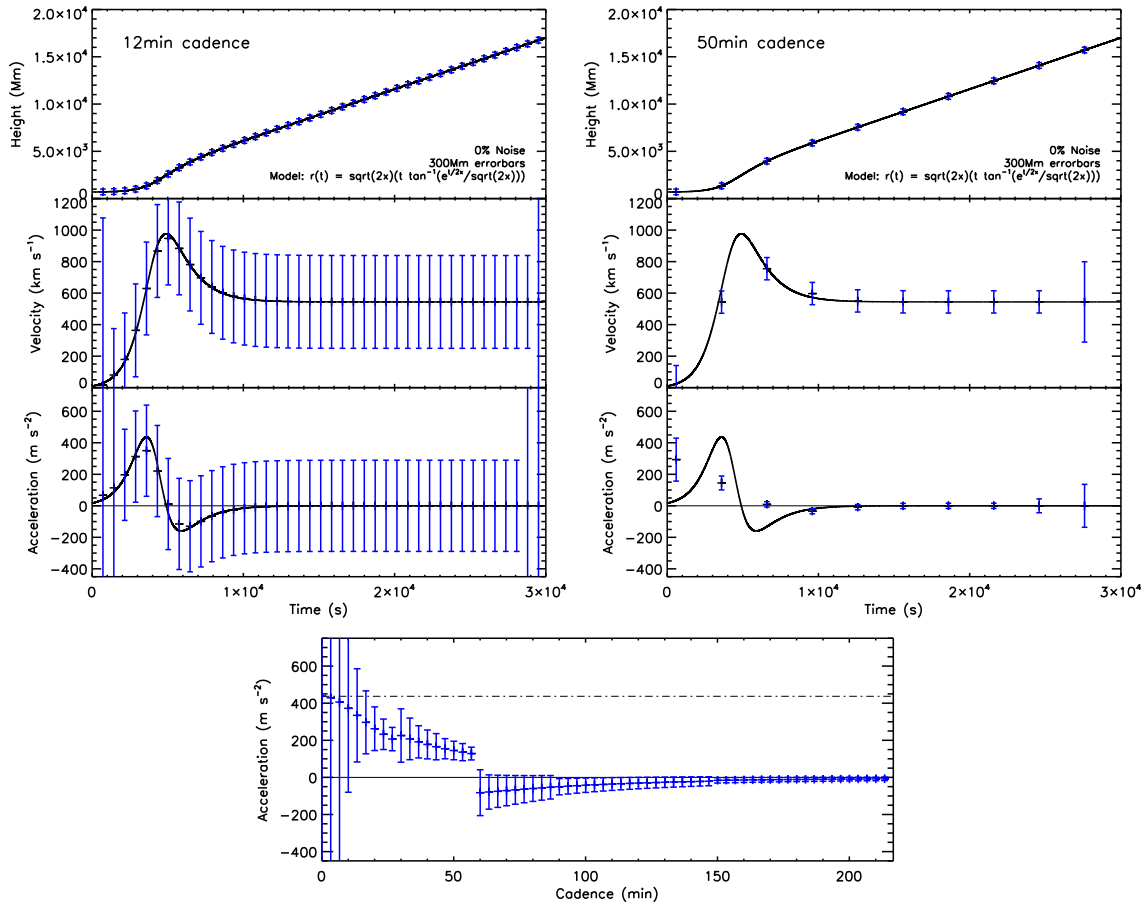


Fig. 3. Simulated data (crosses) for noise distributions with widths of $\pm 20\%$ (top), $\pm 10\%$ (middle) and $\pm 5\%$ (bottom) of the data value. In each case, the fit to the data is shown in red with derived kinematics in the bottom right of each panel.

The acceleration profile exhibits an initial peak followed by a deceleration and then leveling to zero. This is akin to a general impulsive CME that undergoes an initial high-acceleration eruptive phase, and then decelerates to match the solar wind speed during its propagation phase. Thus a model CME height-time profile is generated enabling synthetic observation samples to be taken at different cadences (Figure 4).

We investigate the effect of the cadence of the observations on the derivation of the kinematics and associated errorbars using the standard 3-point Lagrangian interpolation. In the first instance fixed 3σ errorbars of ± 300 Mm are applied to the height-time points, without any noise added. This is useful to simply test the effects of the cadence on the derived velocity and acceleration profiles and their associated errors. The top left and right plots of Figure 4 show the model height-time, velocity and acceleration profiles sampled at cadences of 12 and 50 mins respectively. As the cadence is reduced, i.e., the cadence time is increased, the errorbars become smaller due to the inverse dependence of the Lagrangian error terms on the time between the datapoints Δt^{-2} (see Equation 6). However, reducing the cadence reduces the resolution with which the acceleration peak is detectable, and so the acceleration profile is smoothed out. Conversely, the errorbars would become erroneously large for very high-cadence measurements, even though the measurements would better reveal the true trends of the kinematic profiles. This fundamentally implies that the errors do not truly reflect the uncertainty on the data at a given cadence, and are in fact completely redundant.

We further investigate these effects for the case of a coronal wave moving with constant acceleration and observed at

**Fig. 4.**

sampling cadences akin to the instruments EIT (12 mins), EUVI (5 mins) or AIA (12 s). Figure 5 shows examples of these, with a quadratic fit to the sample data with a scatter of $\pm 5\%$. It is clear that the higher-cadence data best resolves the true kinematic profile, providing an accurate estimation of the wave velocity and acceleration.

The variation in derived kinematics with cadence is shown in Figure 6 (again for $\pm 5\%$ uncertainty). As the cadence decreases, the derived velocity and acceleration approach the model values, with the scatter showing a dramatic reduction below ~ 50 s cadence. These results are consistent with the observations made by both Long et al. (2008) and Ma et al. (2009) and show that the effects of image cadence must be accounted for when trying to derive the true kinematics of a CBF pulse.

It is clear that the variation in both noise and imaging cadence can strongly influence the derived kinematics of a CBF pulse, while the different numerical differencing techniques do not return accurate estimates of the pulse kinematics. However, it is possible to use a bootstrapping approach to overcome these issues as this is a statistically significant technique that has been optimised for small data-sets such as those typically obtained when studying CBF pulses.

4. Bootstrapping

Bootstrapping was first proposed by Efron (1979) as a general interpretation of the jackknife, allowing statisti-

cal quantities to be estimated from a limited sample to a high degree of accuracy. In principle this allows a statistical quantity (such as the mean, variance etc.) of a distribution to be estimated using a small sample of measurements from that distribution. The resulting estimates are statistically significant, with statistically defined associated error estimates.

While there are a number of different bootstrapping techniques, each of which is useful for a different purpose, in this case we will be using the residual resampling technique. Whereas the majority of bootstrapping techniques involve removing one point at random and recalculating the fit to the data, this is inappropriate in this case due to the small sample set available. The residual resampling technique however, does not require data-point removal, making it more appropriate for small data-sets such as those available here.

The residual resampling technique works as follows. The distance-time measurements (y_i ; $i = 1, 2, \dots, n$) are first fitted using a quadratic equation of the form

$$r(t) = r_0 + v_0 t + \frac{1}{2} a t^2, \quad (11)$$

where r_0 is the offset distance, v_0 is the initial velocity, a is the constant acceleration of the pulse, and t is the time elapsed since the first observation of the disturbance. This yields the fitted values (\hat{y}_i) and residuals ($\hat{\epsilon} = y_i - \hat{y}_i$) for each point. The residuals are then randomly ordered and randomly assigned a sign (1 or -1), before being added

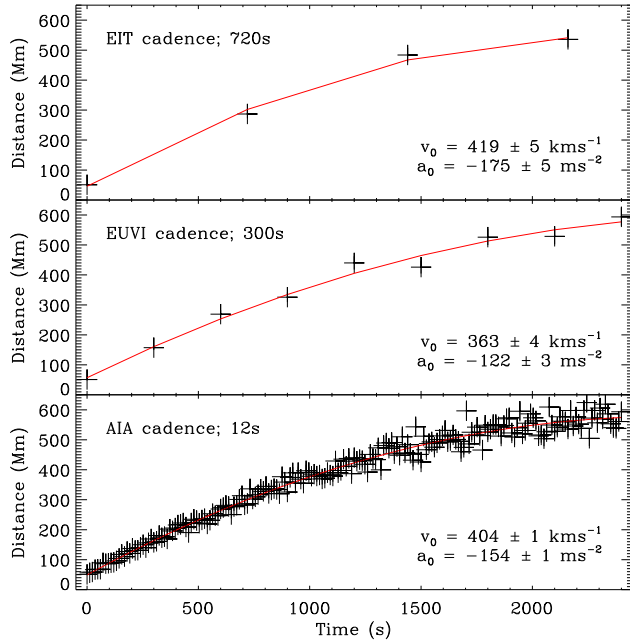


Fig. 5. Simulated data (crosses) for cadences of 720 s (top; comparable to EIT), 300 s (middle; comparable to EUVI) and 12 s (bottom; comparable to AIA). In each case, the fit to the data is shown in red with derived kinematics in the bottom right of each panel.

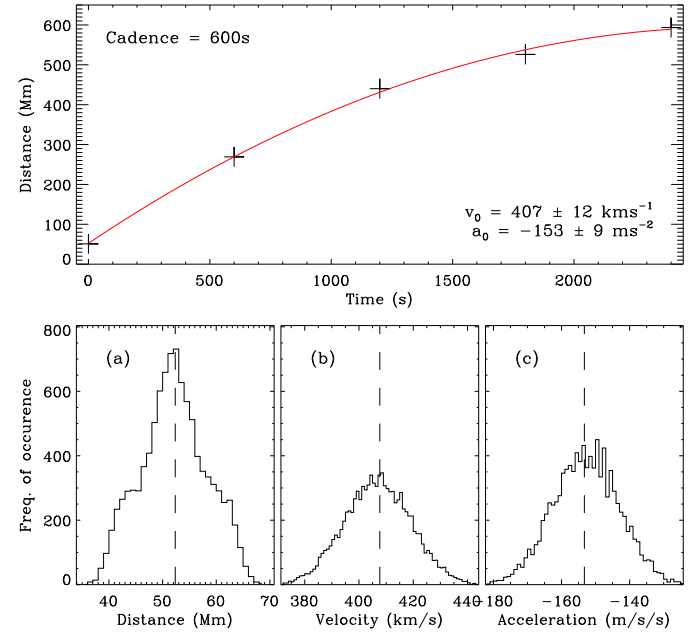


Fig. 7. Top: Simulated data (asterisks) with bootstrapped fit shown in red and parameters in bottom right. Bottom: Histograms showing the distance (a), velocity (b) and acceleration (c) derived using the bootstrapping technique.

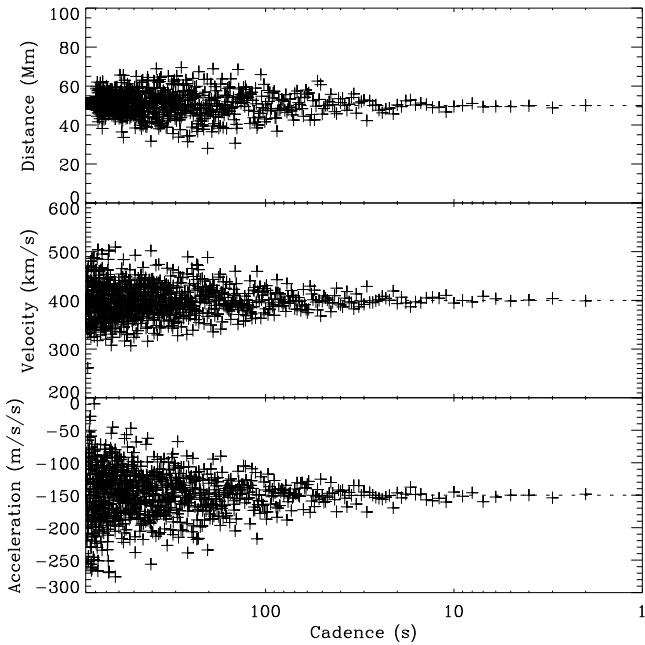


Fig. 6. Derived kinematics for varying image cadence with $\pm 5\%$ uncertainty. Distance, velocity and acceleration are shown in the top, middle and bottom panels respectively, with the x-axis shown using logarithmic scaling to highlight the effects of varying the image cadence.

to the original fit values to produce a new data set. These new data are then fitted using the same model, with the

resulting re-fitted parameters recorded. The process is then repeated a large number of times ($\sim 10\,000$).

This has the effect of repeating the fit to slightly varying data a large number of times, allowing a distribution of fit values to be obtained. The mean and standard deviation of this distribution then provide the estimated value and associated error of the parameter. This technique is statistically rigorous and produces a more accurate result than a simple model fit to the given data.

This technique was applied to the simulated data-set used in Section ?? to allow a comparison of the effectiveness of the bootstrapping approach with the numerical differencing techniques. The results of this analysis are shown in Figure 13. The upper panel here shows the simulated data (indicated by the asterisks) with the bootstrapped fit to the data shown by the red line. The kinematics obtained by the bootstrapping approach are given in the bottom right. The bottom panels (a), (b) and (c) show the histograms for the distance, velocity and acceleration parameters respectively. These histograms returned by the bootstrapping approach for each parameter allow a statistical determination of the fit parameters, a fact reflected in the error term for the derived kinematics.

The kinematics returned by the bootstrapping approach match the model kinematics within one standard deviation, while also producing an accurate estimate with well-defined errors, unlike those of the numerical differencing techniques. It should also be noted that none of the data-points have been removed, unlike the majority of the numerical differencing techniques tested.

As a result of the simulations carried out to test the different approaches to determining the kinematics of a CBF pulse, the residual resampling bootstrapping technique was chosen as the best method. This fits a model directly to the distance-time measurements, allowing the kinematics

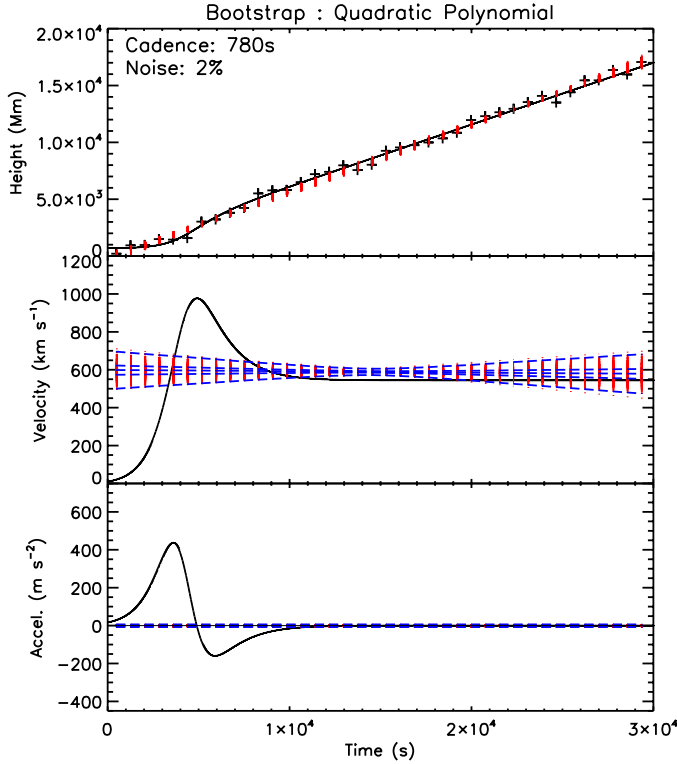


Fig. 8. Top: Simulated data (asterisks) with bootstrapped fit shown in red and parameters in bottom right. Bottom: Histograms showing the distance (a), velocity (b) and acceleration (c) derived using the bootstrapping technique.

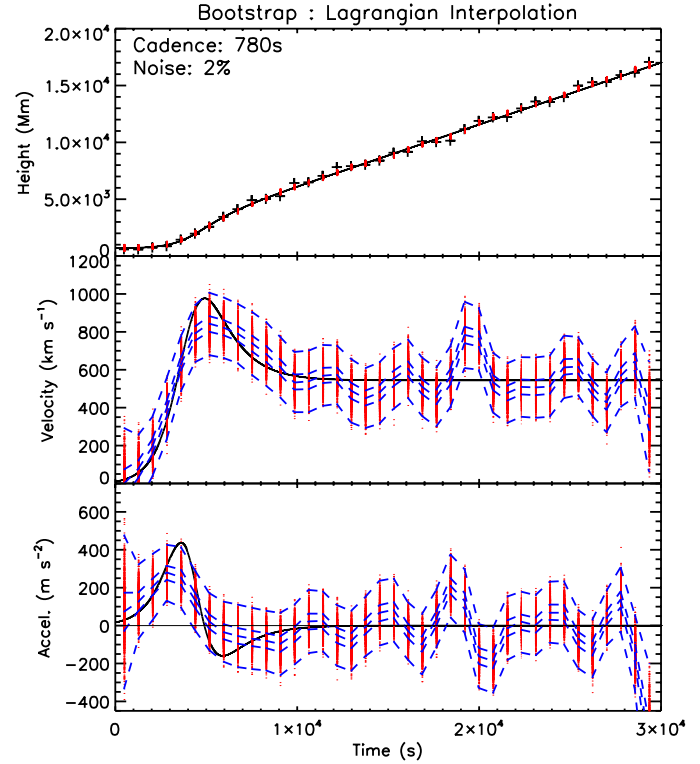


Fig. 10. Top: Simulated data (asterisks) with bootstrapped fit shown in red and parameters in bottom right. Bottom: Histograms showing the distance (a), velocity (b) and acceleration (c) derived using the bootstrapping technique.

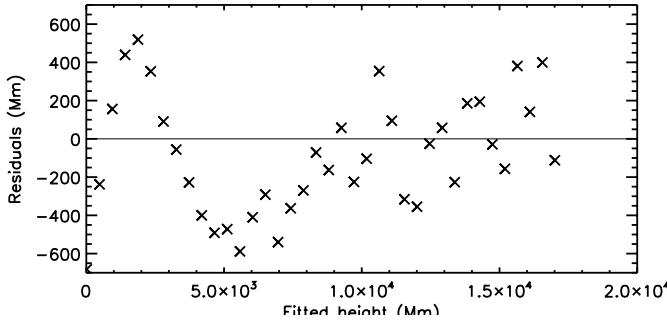


Fig. 9. Top: Simulated data (asterisks) with bootstrapped fit shown in red and parameters in bottom right. Bottom: Histograms showing the distance (a), velocity (b) and acceleration (c) derived using the bootstrapping technique.

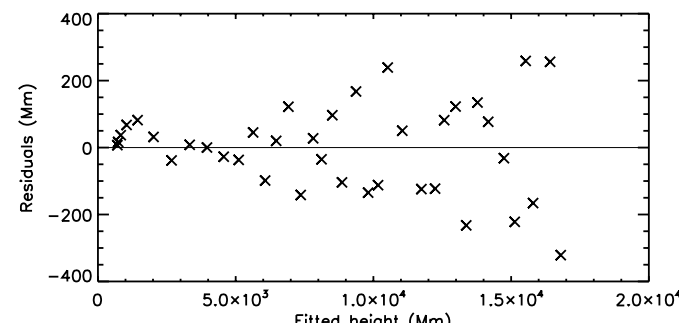


Fig. 11. Top: Simulated data (asterisks) with bootstrapped fit shown in red and parameters in bottom right. Bottom: Histograms showing the distance (a), velocity (b) and acceleration (c) derived using the bootstrapping technique.

of the CBF pulse to be determined to a high degree of accuracy. The kinematics given for each future event studied here therefore reflects the mean value of the bootstrapped distribution, with the associated error given by the standard deviation.

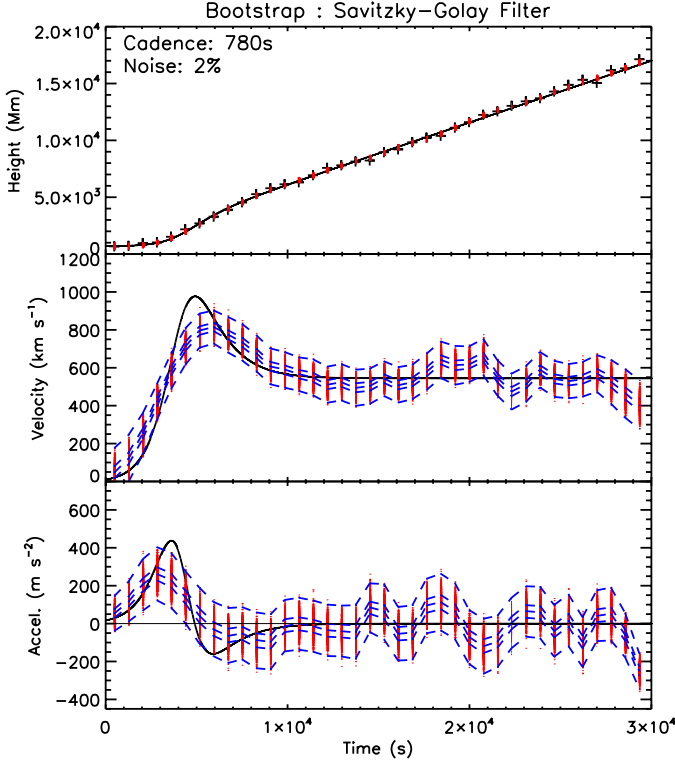


Fig. 12. *Top:* Simulated data (asterisks) with bootstrapped fit shown in red and parameters in bottom right. *Bottom:* Histograms showing the distance (a), velocity (b) and acceleration (c) derived using the bootstrapping technique.

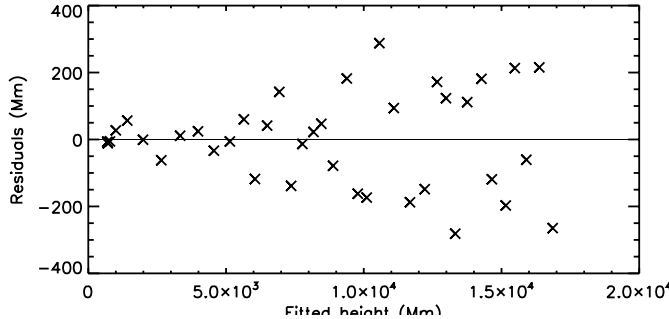


Fig. 13. *Top:* Simulated data (asterisks) with bootstrapped fit shown in red and parameters in bottom right. *Bottom:* Histograms showing the distance (a), velocity (b) and acceleration (c) derived using the bootstrapping technique.

5. Case Studies

5.1. CORIMP

5.2. CorPITA

6. Conclusions

Acknowledgements. This work is supported by SHINE grant 0962716 and NASA grant NNX08AJ07G to the Institute for Astronomy.

The SOHO/LASCO data used here are produced by a consortium of the Naval Research Laboratory (USA), Max-Planck-Institut fuer Aeronomie (Germany), Laboratoire d'Astronomie (France), and the University of Birmingham (UK). SOHO is a project of international cooperation between ESA and NASA. The STEREO/SECCHI project is an international consortium of the Naval Research Laboratory (USA), Lockheed Martin Solar and Astrophysics Lab (USA), NASA Goddard Space Flight Center (USA), Rutherford Appleton Laboratory (UK), University of Birmingham (UK), Max-Planck-Institut für Sonnen-systemforschung (Germany), Centre Spatial de Liege (Belgium), Institut d'Optique Théorique et Appliquée (France), and Institut d'Astrophysique Spatiale (France).

References

- Byrne, J. P., Gallagher, P. T., McAteer, R. T. J., & Young, C. A. 2009, *A&A*, 495, 325
- Byrne, J. P., Morgan, H., Habbal, S. R., & Gallagher, P. T. 2012, *ApJ*, 752, 145
- Chen, P. F., & Wu, Y. 2011, *ApJ*, 732, L20
- Efron, B. 1979, *Ann. Stat.*
- Gallagher, P. T., & Long, D. M. 2011, *Space Sci. Rev.*, 158, 365
- Howard, T., ed. 2011, *Astrophysics and Space Science Library*, Vol. 376, *Coronal Mass Ejections*
- Illing, R. M. E., & Hundhausen, A. J. 1985, *J. Geophys. Res.*, 90, 275
- Lin, C., Gallagher, P. T., & Raftery, C. L. 2010, *A&A*, 516, A44+
- Long, D. M., Gallagher, P. T., McAteer, R. T. J., & Bloomfield, D. S. 2008, *ApJ*, 680, L81
- . 2011, *A&A*, 531, A42
- Ma, S., Wills-Davey, M. J., Lin, J., et al. 2009, *ApJ*, 707, 503
- Morgan, H., Byrne, J. P., & Habbal, S. R. 2012, *ApJ*, 752, 144
- Muhr, N., Veronig, A. M., Kienreich, I. W., Temmer, M., & Vršnak, B. 2011, *ApJ*, 739, 89
- Patsourakos, S., & Vourlidas, A. 2012, *Sol. Phys.*, 93
- Podladchikova, O., Vuets, A., Leontiev, P., & van der Linden, R. A. M. 2012, *Sol. Phys.*, 276, 479
- Schrijver, C. J., Aulanier, G., Title, A. M., Pariat, E., & Delannée, C. 2011, *ApJ*, 738, 167
- Shen, Y., & Liu, Y. 2012, *ApJ*, 754, 7
- Thompson, B. J., & Myers, D. C. 2009, *ApJS*, 183, 225
- Veronig, A. M., Muhr, N., Kienreich, I. W., Temmer, M., & Vršnak, B. 2010, *ApJ*, 716, L57
- Veronig, A. M., Temmer, M., & Vršnak, B. 2008, *ApJ*, 681, L113
- Warmuth, A., & Mann, G. 2011, *A&A*, 532, A151
- Warmuth, A., Vršnak, B., Magdalenić, J., Hanslmeier, A., & Otruba, W. 2004, *A&A*, 418, 1101
- Webb, D. F., & Howard, T. A. 2012, *Living Reviews in Solar Physics*, 9, 3
- Wen, Y., Maia, D. J. F., & Wang, J. 2007, *ApJ*, 657, 1117
- Yashiro, S., Gopalswamy, N., Michalek, G., et al. 2004, *Journal of Geophysical Research (Space Physics)*, 109, 7105
- Zheng, R., Jiang, Y., Yang, J., et al. 2012, *ApJ*, 753, 112